ACS APPLIED MATERIALS & INTERFACES

Research Article

www.acsami.org

Design of Low Pt Concentration Electrocatalyst Surfaces with High Oxygen Reduction Reaction Activity Promoted by Formation of a Heterogeneous Interface between Pt and CeO_x Nanowire

Shipra Chauhan,[†,‡] Toshiyuki Mori,[*,†,‡] Takuya Masuda,[†,‡] Shigenori Ueda,[§,∥] Gary J. Richards,[†,⊥] Jonathan P. Hill,[⊥] Katsuhiko Ariga,[⊥] Noriko Isaka,[#] Graeme Auchterlonie,[▽] and John Drennan[▽]

[†]Global Research Center for Environment and Energy Based on Nanomaterials Science (GREEN) and [⊥]WPI Center for Materials Nanoarchitectonics (MANA), National Institute for Materials Sciences (NIMS), 1-1 Namiki, Ibaraki 305-0044, Japan

[‡]Graduate School of Chemical Sciences and Engineering, Hokkaido University, Kita 13, Nishi 8, Kita-Ku Sapporo, Hokkaido 060-8628, Japan

[§]Synchrotron X-ray Station at SPring-8, NIMS, Sayo, Hyogo 679-5148, Japan

[∥]Quantum Beam Unit, NIMS, 1-2-1 Sengen, Ibaraki 305-0044, Japan

[#]Transmission Electron Microscopy Station, NIMS, 1-2-1, Sengen, Ibaraki 305-0047, Japan

[▽]Centre for Microscopy and Microanalysis, The University of Queensland, St. Lucia, Brisbane, Queensland 4072, Australia

Supporting Information

ABSTRACT: Pt-CeO_x nanowire (NW)/C electrocatalysts for the improvement of oxygen reduction reaction (ORR) activity on Pt were prepared by a combined process involving precipitation and coimpregnation. A low, 5 wt % Pt-loaded CeO_x NW/C electrocatalyst, pretreated by an optimized electrochemical conditioning process, exhibited high ORR activity over a commercially available 20 wt % Pt/C electrocatalyst although the ORR activity observed for a 5 wt % Pt-loaded CeO_x nanoparticle (NP)/C was similar to that of 20 wt % Pt/C. To investigate the role of a CeO_x NW promotor on the enhancement of ORR activity on Pt, the Pt-CeO_x NW interface was characterized by using hard X-ray photoelectron spectroscopy (HXPS), transmission electron microscopy (TEM), and electron energy loss spectroscopy (EELS). Microanalytical data obtained by these methods were discussed in relation to atomistic simulation performed on the interface structures. The combined techniques of HXPS, TEM-EELS, and atomistic simulation indicate that the Pt-CeO_x NW interface in the electrocatalyst contains two different defect clusters: Frenkel defect clusters (i.e., $2Pt_i^{\bullet\bullet}$ - $4O_i''$ - $4V_o^{\bullet\bullet}$ - V_{Ce}'''') formed in the surface around the Pt-CeO_x NW interface and Schottky defect clusters (i.e., (Pt_{Ce}'' - $2V_O^{\bullet\bullet}$ - $2Ce_{Ce}'$) and (Pt_{Ce}'' - $V_O^{\bullet\bullet}$)) which appear in the bulk of the Pt-CeO_x NW interface similarly to Pt-CeO_x NP/C. It is concluded that the formation of both Frenkel defect clusters and Schottky defect clusters at the Pt-CeO_x NW heterointerface contributes to the promotion of ORR activity and permits the use of lower Pt-loadings in these electrocatalysts.

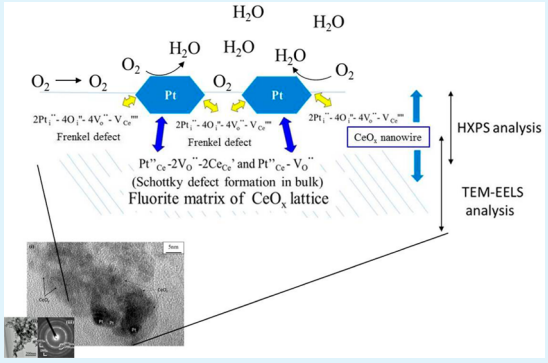

KEYWORDS: *Pt-CeO_x nanowire/C cathode, ORR, Frenkel type defect cluster formation, heterointerface of Pt and CeO_x nanowire, HXPS analysis, EELS analysis*

1. INTRODUCTION

Fuel cell devices can be used to convert chemical energy into electrical energy with high efficiency of power generation and minimal pollutant emission. The development of polymer electrolyte membrane fuel cells (PEMFCs) has been the subject of particular interest for use in residential scale cogeneration systems and vehicular applications.[1−3] For these purposes, and to reduce the cost of electrocatalysts, the improvement of oxygen reduction reaction (ORR) activity on Pt is of great importance.

Recently, nonplatinum cathodes such as carbon-based materials (e.g., N-doped carbon nanotube arrays,[4] Fe−N codoped carbon,[5] free-standing N-doped carbon nanofiber,[6] N-doped graphene,[7] graphene-based carbon nitride nanosheets,[8] S-doped graphene,[9] graphene oxide,[10] N-doped carbon nanocable[11]) have been investigated for PEMFC applications. For PEMFCs, however, the most suitable electrocatalysts are nanosized Pt particles loaded on carbon supports. The reason for that is their reliable ORR activity and stability under different operating conditions. In contrast, there are still several disadvantages of these catalysts that require attention. For cathode catalysts, (1) first, OH adsorption on the Pt particles

Received: December 21, 2015
Accepted: March 23, 2016
Published: March 23, 2016

DOI: 10.1021/acsami.5b12469
ACS Appl. Mater. Interfaces 2016, 8, 9059−9070

inhibits ORR. The resulting slow kinetics of ORR at the Pt surface significantly increases the overpotential and detrimentally affects the performance of PEMFCs.[12,13] (2) Second, after first step oxidation of the Pt surface by adsorption of OH spices, the atomic oxygen was formed by further oxidation of adsorbed OH on the Pt surface. This inert oxide layer easily develops on the nanosized Pt under fuel cell reaction conditions. That surface oxidation on Pt leads to a sluggish ORR activity on the surface of Pt, and an excessive overpotential is required to overcome this inhibition to performance.[14,15] (3) Third, severe conditions (such as low pH) on the cathodic side can cause the agglomeration of nanosized Pt particles by a dissolution-reprecipitation process which leads to an accelerated deactivation of the electrocatalysts.[16,17]

An effective technique to overcome these disadvantages is by modifying the Pt/C electrocatalysts with an appropriate oxide promoter such as TiO_2,[18] WO_3,[18,19] MoO_2,[20] NbO_2,[21] SnO_2,[22,23] or CeO_2.[24−36] In the literature, oxide promoters have been used to improve adsorption characteristics for hydrogen and oxygen at the surface of platinum.[18,22,23] For instance, in the case of the NbO_2 promoter, OH adsorption on Pt was attenuated as a result of the lateral repulsion between PtOH and the oxide surface species.[21] Additionally, the agglomeration of Pt particles under the prevailing acidic conditions could be suppressed by the strong interaction between the oxide promoter and Pt.[19,20]

In the Pt-metal oxide promoter series of electrode materials, Pt-cerium oxide (CeO_x)/C is a unique system compared to other Pt-metal oxide/C electrocatalysts because of the possible variable valence states of the Ce cations in CeO_x in addition to the high oxygen storage capacity of CeO_x. The initial specification for the design of the CeO_x promoter effect in the Pt-CeO_x/C systems was targeted toward direct methanol fuel cells (DMFCs). Since methanol tolerance is one of the important properties of electrocatalysts with high ORR activity from the viewpoint of the methanol crossover effect, the promotion effect of CeO_x in Pt-CeO_x/C is briefly introduced in this Introduction.

The anode performances of Pt-CeO_x/C for DMFCs application were examined and described in the previously published papers.[20−25] The stable anode performance of Pt−CeO_x/C in an alkaline media such as a mixed solution of alcohol and KOH was first reported by Xu et al.[24−26] Alternatively, Takahashi et al. recorded the initial experiments of the anode performance of Pt−CeO_x nanoparticles (NP) on carbon (Pt−CeO_x NP/C) in an acidic media from the perspective of fuel cell applications. They observed a stable anode performance for Pt−CeO_x NP/C and a high activity for the methanol electro-oxidation reaction (MOR) on Pt−CeO_x NP/C electrocatalysts in a mixed aqueous solution of methanol and sulfuric acid.[27−29] They also suggested that the improved anode performance of this system in acidic media was as a result of the high oxygen storage capacity of the CeO_x NP surface, and this is a result of the electrochemical redox reaction between $Ce(Ce^{4+})O_2$ and reduced $Ce(Ce^{4+}, Ce^{3+})O_x$.[28,29]

ORR activity on Pt in Pt−CeO_x NP/C was first examined for the development of DMFC devices by Yu et al.[30] Pt/C cathodes doped with 10 wt % CeO_x NP exhibited a good performance in single cell DMFCs. These workers also proposed the functionalization of CeO_x as a supplier of active oxygen to the Pt surface. Takahashi et al.[31] suggested that the ORR activity at the interface between Pt and CeO_x could be improved by the oxygen storage (i.e., oxygen occlusion) properties of CeO_x on the Pt cathode under the operating conditions of PEMFCs. They proposed that the defect CeO_x lattice converts oxygen molecules into oxide ions (O^{2-}) and the formation of water is activated at the triple phase boundaries of Pt−CeO_x NP/C involving O^{2-}, which can diffuse through the CeO_x lattice, and protons (H^+) which diffuse from the anode side to the cathode side through the polymer membrane electrolyte. In other related work, Lim et al. suggested that active oxygen supplied from CeO_x to the Pt surface contributes to the improvement of the ORR activity of Pt−CeO_x NP/C cathodes. They also examined the durability of ORR activity on Pt−CeO_x NP/C cathodes and demonstrated fuel cell activity using their Pt−CeO_x NP/C material. This work represents the first report revealing the good durability of ORR activity on a Pt−CeO_x NP/C cathode and introduced the prospects for practical use of Pt−CeO_x NP/C in fuel cells.[32,33] However, while this work illustrated the unique aspects and excellent ORR activity at the surface/interface of Pt−CeO_x NP/C, there is generally a lack of clear evidence to explain the role of the CeO_x NP promoter in the enhancement of ORR activity on Pt.

Ou et al. observed the Pt-CeO_x interface structure at Pt particles by using high resolution-transmission electron microscopy (HR-TEM) including a comparison of the key defect structure of the Pt-CeO_x NP interface before and after electrochemical pretreatment processing.[34,35] Their work indicated the clear formation of the oxygen defect structure at the Pt-CeO_x NP interface and that MOR activity on the Pt-CeO_x NP/C anode is improved by formation of a Pt-CeO_x NP interface. In addition, Masuda et al. examined the interfacial reactions on Pt with the Pt-CeO_x NP interface by using in situ X-ray absorption fine structure (XAFS) analysis.[37] Their results suggested that the surface electrochemical oxidation of Pt can be effectively suppressed by using the electrochemical redox reaction of CeO_x at the Pt-CeO_x NP interface and that ORR activity on a Pt-CeO_x NP/C cathode could be enhanced by using the aforementioned unique properties of CeO_x even at room temperature. Based on this data, Fugane et al. fabricated materials containing small amounts of CeO_x loaded on Pt by using an electrochemical pretreatment process and examined both of the ORR activity of Pt−CeO_x NP/C and its fuel cell performance.[38] They optimized the conditions of the electrochemical pretreatment process for maximization of ORR activity on Pt in Pt-CeO_x NP/C and observed high ORR activity with good durability at the surface of their electrocatalysts.[39] They also fabricated a Pt-CeO_x thin film electrode on a conductive Nb-doped $SrTiO_3$ single crystal substrate by using a stepwise process involving pulse laser deposition for the fabrication of an epitaxially grown CeO_x film followed by an impregnation step to load the Pt particles on the CeO_x film.[40] Electrochemical measurements on the Pt-CeO_x thin film electrode clearly revealed the promoting effect of CeO_x. Analytical TEM observations of the thin film electrode suggested that, in this case, the Pt-CeO_x interface contained Schottky type defects (i.e., combination defect of $Pt_{Ce}'' - V_o^{\bullet\bullet}$ and $Pt_{Ce}'' - 2V_o^{\bullet\bullet} - 2Ce_{Ce}'$). Overall, these various results suggest that the design of a defect structure of the Pt-CeO_x NP interface is key to maximizing the promoting effect of CeO_x NP on Pt.

Since the area of the Pt-CeO_x NP interface formed between Pt and CeO_x NP is small, the electrochemically active surface area (EASA) of the previously reported Pt-CeO_x NP/C materials was low (approximately 26 $m^2\ g_{Pt}^{-1}$),[38] and their

DOI: 10.1021/acsami.5b12469
ACS Appl. Mater. Interfaces 2016, 8, 9059−9070

resulting activities were not sufficiently high enough to be of useful electrocatalyst. To overcome this problem, we have prepared CeO_x nanowires (NW) (rather than the more usually prepared CeO_x NP), and we have subsequently prepared Pt loaded CeO_x NW/C anodes seeking improvements of activity of MOR on Pt. The concept behind the use of CeO_x NW is that the relatively flat and wide surface area of CeO_x NW allows the formation of a nanoreaction space for creation of a more expansive Pt-CeO_x NW interface. Relatively large EASA values were found for Pt loaded CeO_x NW/C (i.e., approximately 150 $m^2\ g_{Pt}^{-1}$) as well as improved MOR activities on Pt-CeO_x NW/C over the previously reported Pt loaded CeO_x NP/C materials.[41] In that work, the authors found that the surface of Pt-CeO_x NW/C is composed mainly of Pt^{2+} and Ce^{4+} species. In contrast, the surface of Pt-CeO_x NP/C is composed mostly of Pt^{2+} and Ce^{3+} species. This difference in surface compositions suggests that the defect structure formed at the Pt-CeO_x NW interface contributes to the enhancement of the promoting effect of CeO_x NW; as a result, there is an improvement of activity of MOR on Pt.

To increase the promoting effect of CeO_x NW on the Pt electrocatalyst, structural features of the Pt-CeO_x NW interface should be studied in detail: in particular, the relationship between the defect structural features of the Pt-CeO_x NW interface and ORR activity of Pt in the Pt loaded CeO_x NW/C. This requires careful characterization for the development of low Pt concentration cathodes with high performance because of the slow kinetics of the ORR on Pt in cathodic reactions.

In this work, we compare the ORR activities observed for Pt-CeO_x NP/C and Pt-CeO_x NW/C cathodes for lower Pt contents in the Pt-CeO_x system. Also, the surface and bulk regions formed at the Pt-CeO_x NW interfaces have been characterized by using hard X-ray photoelectron spectroscopy (HXPS) and analytical TEM. For interpretation of micro-analytical data, atomistic simulations were also performed, and the defect structural features revealed about the Pt-CeO_x NW interface are described in the Discussion section of this paper.

2. EXPERIMENTAL SECTION

2.1. Preparation of Pt-Loaded CeO_x NP/C and Pt-Loaded CeO_x NW/C. Pt loaded CeO_x NW electrocatalysts were prepared in a stepwise process. The CeO_x NW was synthesized by using an alcothermal process (Morphology of CeO_x NW is shown in Figure S1(a) of the Supporting Information). The starting materials used were commercially available cerium chloride $CeCl_3{\cdot}H_2O$ (Nacalai Tesque Company, Japan), cetyl tetraethylammonium bromide $C_{19}H_{42}BrN$ (CTAB, Wako Pure Chemical Industries, Ltd., Japan), and urea $(H_2N)_2CO$ (Nacalai Tesque Company, Japan). CTAB and $(H_2N)_2CO$ were respectively used as a surfactant for micelle formation and as a base for control of pH during the reaction. CeO_x NW synthesis has been described in a previous paper.[41] To prepare the reference sample, Pt loaded CeO_x NP electrocatalyst was prepared in a similar stepwise process. CeO_x NP was prepared using the ammonia carbonate precipitation method. Details of the CeO_2 NP synthesis has been described previously.[38]

For impregnation of nanosized Pt particles into CeO_x NW or CeO_x NP, potassium tetrachloroplatinate hydrate ($K_2PtCl_4{\cdot}xH_2O$; Sigma-Aldrich Ltd., Japan) was dissolved in distilled water. The resulting solution was added to a suspension of CeO_x NW or CeO_x NP dispersed in distilled water which had been prepared in advance. The mixture was allowed to stand at room temperature for 12 h. The mixture was then subjected to a reduction step at room temperature for 1 h involving the addition of aqueous sodium borohydride ($NaBH_4$) solution. The suspension was then filtered, and the filtrate was rinsed with distilled water and then ethanol followed by drying at room temperature in a nitrogen atmosphere. In the final stage, the prepared Pt-CeO_x NW (or Pt-CeO_x NP) and conductive carbon (C, Vulcan XC-72R, Cabot Co.) were dispersed in ethanol and dried in a N_2 gas flow for 2 days.

2.2. Characterization of Electrocatalysts. The chemical compositions of the Pt-CeO_x NW/C and Pt-CeO_x NP/C were determined by using inductively coupled plasma-mass spectrometry (ICP-MAS) following the electrochemical pretreatment (described in Section 2.3).

The surface chemical states of Pt loaded CeO_x NW/C were analyzed by using soft X-ray photoelectron spectroscopy (SXPS) with an Al Kα light source. To characterize the average chemical states of deep surface regions of the electrocatalyst, we also used HXPS. HXPS experiments were performed at the undulator beamline BL15XU of the synchrotron facility, SPring-8. The photon energy was set to 5953 eV (inelastic mean free path of photoelectrons from Ce 3d of CeO_2 was estimated to be 7.1 nm[42]). The photoelectrons were detected and analyzed for their kinetic energy using a high-resolution electron analyzer (VG Scienta R4000- 10 kV). Total energy resolution was set to 240 meV. Details of the experimental setup were described elesewhere.[43,44] The binding energy of Pt 4f and Ce 3d core level peaks were corrected using the binding energy of the C 1s core level peak as 284.5 eV. Peak separation analysis was performed using software UNIFIT2014 (Leipzig University, Germany). A detailed description of the process of estimating the Ce^{3+}/Ce^{4+} ratio is given elsewhere.[40]

The morphologies and microstructures of the samples were characterized by TEM. TEM observation was performed at an electron accelerating voltage of 200 kV (JEOL JEM-2100F and JEM-2000EX). Local chemical analysis was performed by using the electron energy loss spectroscopy (EELS) facility of the TEM instrument used here (JEOL JEM-2100F). In addition, selected area electron diffraction analysis was used for identification of crystal phases at the TEM analysis scale. Also, the crystalline phases of 5 wt % Pt loaded CeO_x NP/C and 5 wt % Pt loaded CeO_x NW/C were characterized by using X-ray diffraction (XRD) analysis (Rigaku instrument RINT Ultima plus 2000).

2.3. Electrochemistry of the Electrocatalysts. The cathode properties of Pt-CeO_x NW/C were examined by using cyclic voltammetry in 0.5 M aqueous H_2SO_4 solution in the potential range from 0 to 0.8 V (vs Ag/AgCl). Water was purified using an RO (reverse osmosis)−EDI (electro-deionization) system (MILLPORE, Elix Advantage, Japan), and ultrapure grade H_2SO_4 (Kishida Chemicals Company, Japan) was used for preparation of the electrolyte solution. Electrochemical measurements were carried out (after electrochemical pretreatment at 28 °C) in a 0.5 M aqueous H_2SO_4 solution using a standard three-electrode glass cell with a rotating disk electrode. Pt foil and Ag/AgCl were used as counter and reference electrodes, respectively. Samples for electrochemical measurement were prepared from a suspension of the electrocatalysts (2 mg mL^{-1}) in ethanol solution. The suspension was spread onto the surface of a glassy carbon electrode (area: 0.385 cm^2) using a micropipette. The amount of electrocatalyst suspension applied to the glassy carbon electrode was 5 μL. All potentials measured were converted to the reversible hydrogen electrode (RHE) scale. To evaluate the ORR activity, the electrolyte solution was saturated with N_2 or O_2 by passing ultrapure N_2 or ultrapure O_2 gas for at least 1 h to obtain an N_2-saturated or O_2-saturated environment before electrochemical measurements. Final hydrodynamic voltammetric curves were determined by subtraction of the observed hydrodynamic voltammograms in N_2-saturated electrolyte solution from the observed hydrodynamic voltammograms in O_2-saturated electrolyte solution at each rotation rate (i.e., 2000, 1500, 1250, and 1000 rpm). For electrochemical measurements, the potential was swept from the positive to the negative side at a sweep rate of 10 mV s^{-1}. For comparative purposes, the same amount of each catalyst by mass was loaded onto the glassy carbon rotation disk electrode, and the geometric surface area was calculated by using Levich's equation (sweep rate: 10 mV s^{-1}). The current density was estimated using the geometric surface area.

DOI: 10.1021/acsami.5b12469
ACS Appl. Mater. Interfaces 2016, 8, 9059−9070

For a comparison of cathode properties with a commercially available sample, the ORR activity observed for Pt/C (Johnson Matthey Co., HiSPEC 8000) was also examined. Prior to electrochemical measurements, an electrochemical pretreatment for conditioning of the Pt loaded CeO_x NW/C and commercially available Pt loaded C surfaces was carried out by applying 300 cycle sweeps and 50 cycle sweeps in the potential ranging from 0.0 to 1.3 V (vs Ag/AgCl), respectively. The sweep rate for the conditioning process was 50 mV s^{-1}. Note that the $Ce(OH)_3$ layer covered the surface of the CeO_x NW surface with Pt species during the reduction process (see Figure S1(b) of the Supporting Information). The Pt species was in between the CeO_x NW surface and the $Ce(OH)_3$ layer. Since the CeO_x NW surface and the $Ce(OH)_3$ layer have a basic nature and $K_2PtCl_4{\cdot}xH_2O$ has an acidic nature, the strong interaction between Pt and CeO_x NW would happen by this acid−base interaction on CeO_x NW. On the other hand, the surface of the Pt loaded CeO_x NW surface was covered by a thick impurity layer (i.e., $Ce(OH)_3$) as shown in Figure S1(b) of the Supporting Information. Before measurement of ORR on Pt loaded CeO_x NW/C, the aforementioned electrochemical pretreatment process is important in order to remove the impurity layer from the surface of the electrocatalyst. This set of experiments provided confirmation of the steady state condition and resulted in obtaining reliable comparison of measurement data of electrode performance. Also, the stability of ORR of Pt loaded CeO_x NW/C and commercially available Pt loaded C was examined by using a long cycle test up to 1000 cycle sweeps.

To determine the number of electrons transferred during ORR on Pt-CeO_x NW/C, the Kotecky−Levich (K-L) plots were used. Tafel plots derived from the intercepts of K-L plots at various potential were used for a comparison of ORR activity of the electrocatalysts.

2.4. Atomistic Simulation. To assess the influence of the defect structure at the interface of Pt-CeO_x NW on its cathodic properties, atomistic simulations were performed. The lattice energy is the sum of long-range Coulombic interactions and short-range interactions described by parametrized pair potentials, S_{ij}. Short-range interactions were modeled using a Buckingham potential of the form $S_{ij} = A \exp(-r_{ij}/\rho) - Cr_{ij}^{-6}$, where A, ρ, and C are adjustable parameters. The values of these parameters are listed in Table 1.[40,45] The short-range interactions were set to zero beyond a cutoff at 20 Å. The effect of ionic polarizability of O^{2-} and Ce^{4+} ions was included through the shell model.[39,44] In this model, the ions are comprised of a massive core with charge Xlel and a mass-less shell with charge Ylel. The overall charge state of each ion is equal to (X+Y)lel. The core and shell were connected by an isotropic harmonic spring of force constant k. These shell parameters are listed in Table 2.[46] To predict how a lattice accommodates defects, the Mott−Littleton two-region approach was used for the simulation of the defect formation energy, which is coded in the General Utility Lattice Program (GULP).[47] In the simulation used here, the lattice for energy minimization was partitioned into two regions: a spherical inner region I, at the center of which the defects were introduced, and an outer region II, which extends to infinity. To ensure a smooth transition between regions I and II, an interfacial region IIa was introduced. In the present work, we used an inner region I with a radius of $3.0a_0$ (a_0 is 5.411 Å, which is the lattice constant of CeO_2) and an interfacial region IIa with a radius of $6.0a_0$. To calculate the intrinsic defect energy, the Mott-Littleton two-region method was applied. Also, the binding energy ΔE_b was calculated to investigate the preference and stability of defect clusters. It is described as $\Delta E_b = \Sigma E_{isolated} - E_{cluster}$, where $\Sigma E_{isolated}$ is the sum of the defect energy for all individual components and $E_{cluster}$ is the entire defect energy of this cluster. Note that the calculated ΔE_b must have a positive value if the assumed clusters in this modeling are stable.

Table 1. Short-Range Pair Potentials

species	A/eV	ρ/Å	C/eV Å^6
$Ce^{4+}-O^{2-}$	1986.8	0.3511	20.40
$Pt^{2+}-O^{2-}$	2561.61	0.3200	0.00
$O^{2-}-O^{2-}$	22764.3	0.149	45.83

Table 2. Shell Model Parameters

species	Y/e	k/eVÅ^{-2}
Ce^{4+}	7.7	291.8
O^{2-}	−6.1	419.9

3. RESULTS SECTION

3.1. Crystal Phase and Microstructure Observed for Pt-Loaded CeO_x NW/C and Pt-Loaded CeO_x NP/C. The crystal phases observed for electrochemically pretreated 5 wt % Pt loaded CeO_x NW/C and electrochemically pretreated 5 wt % Pt loaded CeO_x NP/C are shown in Figure 1(a) and Figure 1(b), respectively. Values for the crystallite size obtained from these two samples are compared in Table 3. The estimated crystallite size values obtained by using CeO_x (111) and Pt (111) peaks were almost the same between the two samples. In contrast, the intensity of XRD peaks for electrochemically pretreated 5 wt % Pt loaded CeO_x NW/C (Figure 1(a)) were weaker than those of electrochemically pretreated 5 wt % Pt loaded CeO_x NP/C (Figure 1(b)). Since one-dimensional CeO_x NW which consists of CeO_x primary particles is a bulky material, the intensity of the XRD profile taken from 5 wt % Pt loaded CeO_x NW/C was low compared to that of 5 wt % Pt loaded CeO_x NP/C. The morphological features of the bulky CeO_x NW contained in the Pt loaded CeO_x NW/C could be useful as a framework for electrode layers in fuel cells since oxygen (or hydrogen) must diffuse well into the cathode layer (or anode layer) to maintain a high performance of fuel cell devices.

Figure 2 shows the selected area electron diffraction patterns (SAEDPs) and TEM images of electrochemically pretreated 5 wt % Pt loaded CeO_x NW/C (a) and electrochemically pretreated 5 wt % Pt loaded CeO_x NP/C (b). A representative morphology of electrochemically pretreated CeO_x NWs loaded with Pt can be observed in the low magnification TEM images (Figure 2(a)-(ii)) of 5 wt % Pt loaded CeO_x NW/C. During the electrochemical pretreatment process, the morphology of as-prepared CeO_x NW was changed, and the active Pt-CeO_x NW interface came up on the surfaces of the sample. Thus, the electrochemical active surface area (EASA) which can be estimated from the hydrogen desorption from Pt in 5 wt % Pt loaded CeO_x NW/C (159 m^2 g_{Pt}^{-1}) became much higher than commercially available 20 wt % Pt/C (51 m^2 g_{Pt}^{-1}) (see Figure S2(a) of the Supporting Information), while the average particle size of Pt on the aforementioned sample was almost the same as commercially available Pt/C. In high resolution TEM (HR-TEM) images of the same sample, the well-crystalline CeO_x NPs which compose the CeO_x NWs were observed together with nanosized Pt particles as shown in Figure 2(a)-(i). (Particle size distribution of Pt on CeO_x NW is shown in Figure S2(c) of the Supporting Information.) This clearly indicates that Pt NPs are shallowly embedded into the fluorite matrix of CeO_x. The corresponding SAEDP pattern (Figure 2(a)-(iii)) contains diffraction rings assigned to elemental Pt, which can be readily separated from those of the fluorite-structured CeO_x. Diffraction rings as a result of CeO_x are of relatively high intensity indicating that the CeO_x NWs consist of highly crystalline CeO_x NPs. This agrees well with the results of HR-TEM observations.

DOI: 10.1021/acsami.5b12469
ACS Appl. Mater. Interfaces 2016, 8, 9059−9070

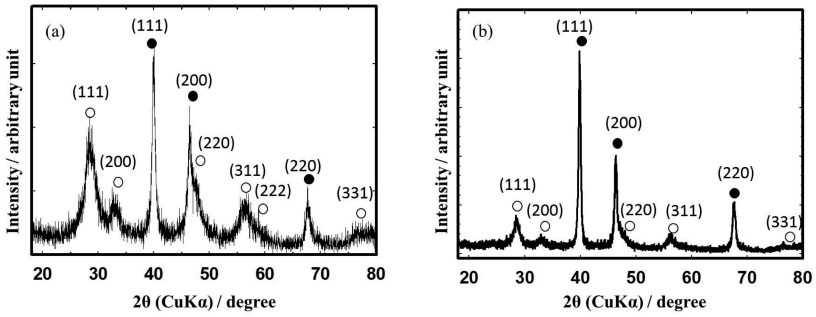

Figure 1. XRD profiles taken from electrochemically pretreated 5 wt % Pt loaded CeO_x NW/C (a) and electrochemically pretreated 5 wt % Pt loaded CeO_x NP/C (b). The closed circle symbol indicates Pt; the open circle symbol indicates CeO_2.

Table 3. Crystallite Size Derived from 5 wt % Pt Loaded CeO_x NW/C and 5 wt % Pt Loaded CeO_x NP/C[a]

	CeO_x (111)	Pt (111)
5 wt % Pt-CeO_x NW/C	4.4 nm	2.1 nm
5 wt % Pt-CeO_x NP/C	5.0 nm	2.2 nm

[a]CeO_x NW: CeO_x nanowire, CeO_x NP: CeO_x nanoparticle.

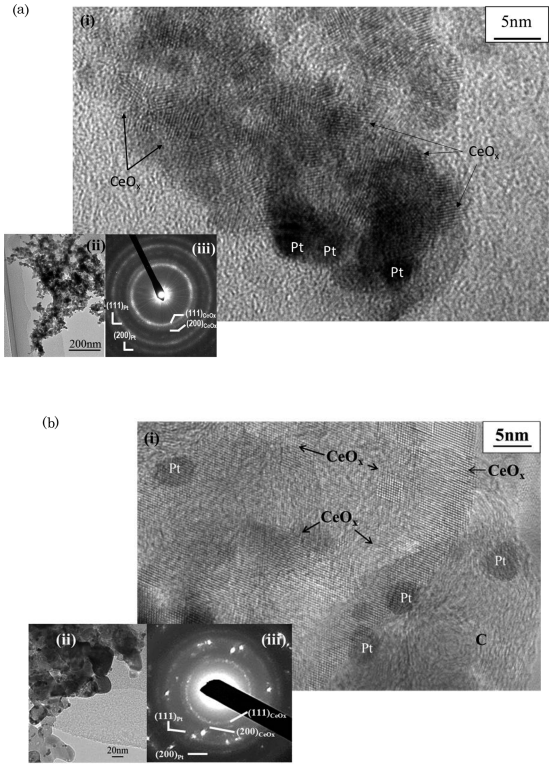

Figure 2. HR-TEM images taken from 5 wt % Pt-CeO_x nanowire/C ((a)-(i)) and 5 wt % Pt-CeO_x nanoparticle/C ((b)-(i)) after electrochemical pretreatment. Insets are low magnification TEM images taken from 5 wt % Pt-CeO_x nanowire/C ((a)-(ii)), 5 wt % Pt-CeO_x nanoparticle/C ((b)-(ii)) and SAEDPs recorded from 5 wt % Pt-CeO_x nanowire/C ((a)-(iii)) and 5 wt % Pt-CeO_x nanoparticle/C ((b)-(iii)).

In contrast, microstructural features of 5 wt % Pt loaded CeO_x NP/C revealed agglomerated CeO_x NPs in low resolution TEM images (Figure 2(b)-(ii)). The HR-TEM image (Figure 2(b)-(i)) indicates that Pt NPs are situated both on crystalline CeO_x and amorphous carbon. Also, the observed intensity of diffraction rings of CeO_x was low relative to the CeO_x NW sample (see Figure 2(a)-(ii)). This suggests that the crystallinity of CeO_x NP is lower than that of CeO_x NW. On the basis of microanalytical results for both 5 wt % Pt loaded CeO_x NW/C and 5 wt % Pt loaded CeO_x NP/C, it was concluded that the metal–support interaction in Pt loaded CeO_x NW/C is much greater than that in Pt loaded CeO_x NP/C.

3.2. Oxygen Reduction Reaction (ORR) Activity.

Hydrodynamic voltammograms of ORR observed for commercially available 20 wt % Pt loaded C (i) and 5 wt % Pt loaded CeO_x NW/C (ii) cathodes are shown in Figure 3. Also, the

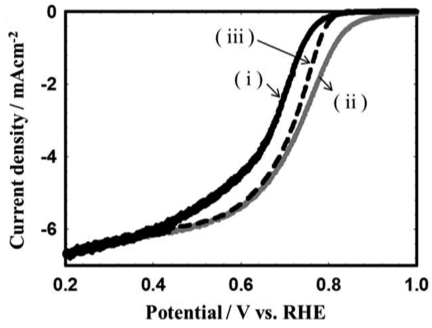

Figure 3. Hydrodynamic voltammograms of ORR observed for commercially available 20 wt % Pt/C (i), 5 wt % Pt-CeO_x NW/C (ii), and 20 wt % Pt-CeO_x NP/C from ref 39 (iii).

previously reported hydrodynamic voltammogram observed for 20 wt % Pt loaded CeO_x NP/C was demonstrated in this figure by using a dashed line (i.e., (iii) in Figure 3) as reference data. The hydrodynamic voltammogram observed for 5 wt % Pt-CeO_x NW/C after electrochemical pretreatment from 0 to 1.5 V (vs RHE) is shifted to a higher potential compared to the electrochemically pretreated 20 wt % Pt/C. To characterize those hydrodynamic voltammograms clearly, the onset potentials and half-wave potentials observed for commercially available Pt/C, previously reported 20 wt % Pt loaded CeO_x NP/C, and electrochemically pretreated 5 wt % Pt-CeO_x NW/C were summarized in Table 4. Both onset potentials and half-wave potentials observed for 5 wt % Pt-CeO_x NW/C were higher than the other two electrocatalysts. Those clearly indicate that ORR activity of 5 wt % Pt loaded CeO_x NW/C is conspicuously higher than that of the commercially available 20 wt % Pt loaded C as demonstrated in Figure 3 and Table 4.

Since the four electron reduction reaction of O_2 to H_2O involved in ORR on the 5 wt % Pt-CeO_x NW/C cathode is important in the fuel cell reaction, the number of electrons involved in the cathode reaction was examined by using

DOI: 10.1021/acsami.5b12469
ACS Appl. Mater. Interfaces 2016, 8, 9059–9070

Table 4. Half-Wave Potential and Onset Potential of ORR Observed for Electrocatalysts[a]

electrocatalysts	half-wave potential/V vs RHE	onset potential/V vs RHE
20 wt % Pt/C (commercial)	0.65	0.79
5 wt % Pt-CeO_x NW/C	0.75	0.89
20 wt % Pt-CeO_x NP/C	0.69	0.80

[a]CeO_x NW: CeO_x nanowire, CeO_x NP: CeO_x nanoparticle.

Kotechky-Levich (K-L) plots, as shown in Figure 4. A plot of i^{-1} vs $\omega^{-1/2}$ (ω: rotation rate of electrode) for various potentials

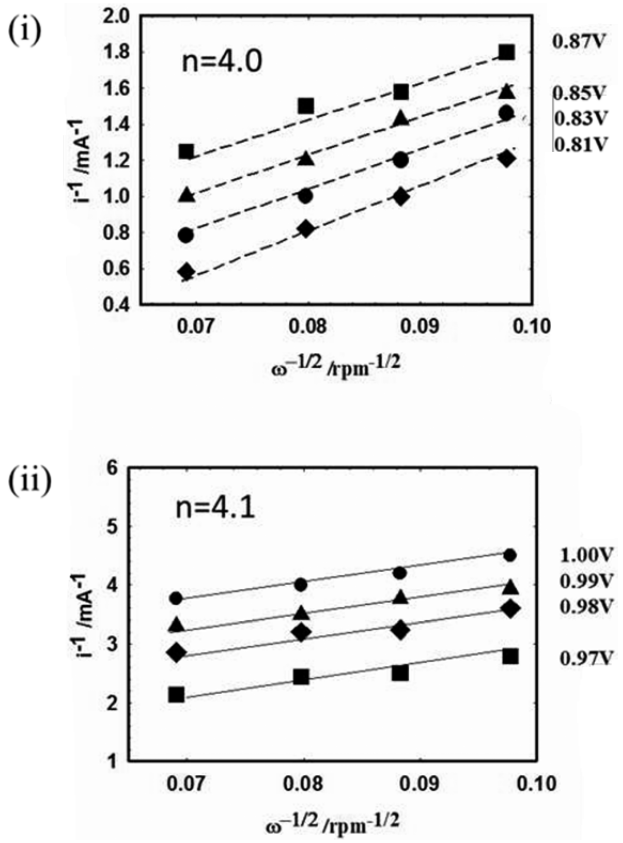

Figure 4. Kotechky-Levich plots derived from 5 wt % Pt-CeO_x NW/C, analysis region: 0.81 to 0.87 V/vs RHE (i) and 0.97 to 1.00 V/vs RHE (ii).

yields straight lines with intercepts corresponding to the kinetic currents (I_k). Their slopes allow an assessment of the number of electrons involved in the ORR. On 5 wt % Pt-CeO_x NW/C, the number of electrons estimated from the slopes of K-L plots was approximately 4.0 as well as for the commercially available 20 wt % Pt/C. This indicates that the standard ORR of the fuel cell cathode reaction was observed for 5 wt % Pt-CeO_x NW/C as well as for the commercially available Pt/C, as shown in Figure 3.

To establish the promoting effect of CeO_x NW on ORR activity of Pt, Tafel plots of 5 wt % Pt-CeO_x NW/C in O_2 saturated 0.5 M aqueous H_2SO_4 solution derived from intercepts of K-L plots at various potentials were compared to those of commercially available 20 wt % Pt/C as shown in Figure 5(a). The Tafel slope of commercially available Pt/C is consistent with the previously published Tafel slopes observed

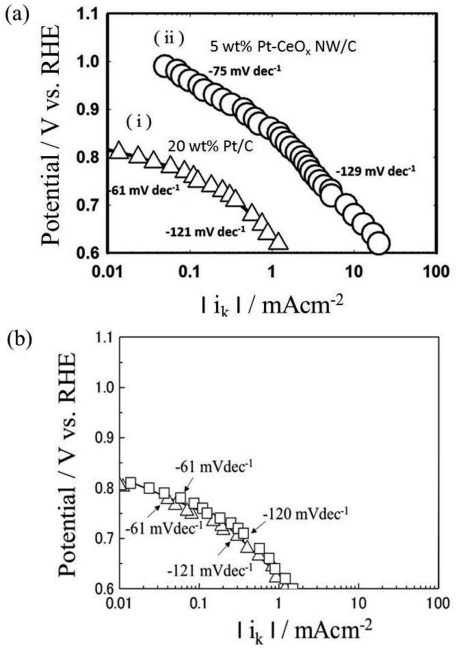

Figure 5. (a) Tafel plots of commercially available 20 wt % Pt/C (i) and 5 wt % Pt-CeO_x NW/C (ii) derived from the intercepts of K-L plots at various potentials, (b) Tafel plots of commercially available 20 wt % Pt/C (△), and 5 wt % Pt-CeO_x NP/C (□) derived from the intercepts of K-L plots at various potentials.

for Pt/C.[48] On the other hand, the kinetic current which corresponds to the horizontal axis of the Tafel plot observed for 5 wt % Pt-CeO_x NW/C shifted to a higher kinetic current region relative to 20 wt % Pt/C. This indicates that ORR activity on Pt is promoted on CeO_x NW in the 5 wt % Pt-CeO_x NW/C, even though Pt content is only 25% of that contained in commercially available Pt/C. Note that the Tafel slope derived from 5 wt % Pt loaded CeO_x NW/C was steeper than that of previously reported 20 wt % Pt-CeO_x NP/C (see Figure S3 of the Supporting Information). In contrast, the Tafel slopes derived from 5 wt % Pt-CeO_x NP/C are similar to those obtained for commercially available 20 wt % Pt/C, as shown in Figure 5(b). In addition, the results of chemical compositional analysis for both 5 wt % Pt-CeO_x NW/C and 5 wt % Pt-CeO_x NP/C agree with the expected compositions as shown in Table 5. On the basis of results contained in Figures 5(a), 5(b) and

Table 5. Chemical Analysis of Elements in Electrochemical Pretreated Electrocatalysts[a]

electrocatalysts	Pt/ wt %	Ce/ wt %	C/ wt %	Ce/Pt/-	Ce/C/-
5 wt % Pt-CeO_x NW/C	5.6	41.7	52.7	7.4	0.8
5 wt % Pt-CeO_x NP/C	5.1	38.0	48.0	7.4	0.8

[a]CeO_x NW: CeO_x nanowire, CeO_x NP: CeO_x nanoparticle.

Tables 4 and 5, it is concluded that the promoting effect of the CeO_x NW surface on the ORR activity of Pt is much greater than that of the CeO_x NP surface.[49]

Since stability of mass activities is one of the important factors for development of electrocatalysts with high ORR activity, the stability of ORR on Pt-CeO_x NW/C and commercially available Pt/C was examined by using the long cycle test. The results of the long cycle test were shown in Figure 6. In this figure, the previously reported data of stability

DOI: 10.1021/acsami.5b12469
ACS Appl. Mater. Interfaces 2016, 8, 9059−9070

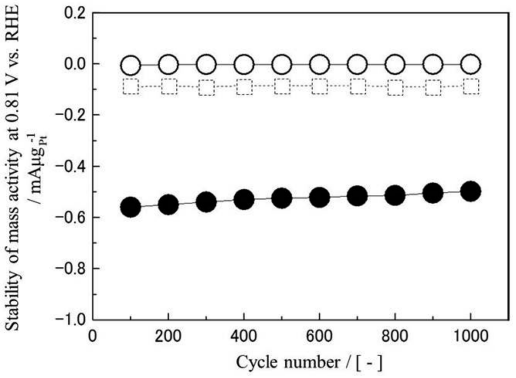

Figure 6. Stability of mass activity in a long cycle test up to 1000 cycle sweeps; closed circle symbols: 5 wt % Pt loaded CeO_x NW/C, solid line open circle symbols: commercially available Pt/C, dashed line square symbols (20 wt % Pt loaded CeO_x NP/C (ref 39)). Sweep rate: 50 mV s^{-1}, potential-range of cycle test: 0 to 1.0 V vs RHE.

of ORR on Pt-CeO_x NP/C was also presented. The mass activity of ORR observed for 20 wt % Pt-CeO_x NP/C and 20 wt % Pt/C in the long cycle test was almost constant up to 1000 cycle sweeps, while those mass activities were not so high at 0.81 V vs RHE (see solid line open circle and dashed line open square symbols). In contrast, the ORR activity of 5 wt % Pt-CeO_x NW/C which is higher than 20 wt % Pt-CeO_x NP/C and 20 wt % Pt/C was stable up to 1000 cycle sweeps, but the mass activity of ORR in the long cycle test slightly decreased in the present work as shown in Figure 6. Approximately 14% decrement of mass activity from 100 cycle sweeps to 1000 cycle sweeps was observed for 5 wt % Pt-CeO_x NW/C. On the other hand, EASA values observed for the same sample were also slightly decreased in the present long cycle test. The initial EASA value was observed for 5 wt % Pt-CeO_x NW/C as approximately 159 $m^2\ g_{pt}^{-1}$. After 1000 cycle sweeps, it was 140 $m^2\ g_{pt}^{-1}$. The decrement of EASA observed for 5 wt % Pt-CeO_x NW/C was around 12%. Since the decreased amount (i.e., about 12%) of EASA almost corresponds to a decrement of mass activity (i.e., about 14%), the small amount of the Pt-CeO_x interface would be resolved from the surface of the electrocatalyst into a 0.5 M H_2SO_4 electrolyte solution in the long cycle test. In the present step of our work, it is supposed that the aforementioned small dissolution of the Pt-CeO_x interface in acidic solution will not affect the performance of membrane electrolyte assembly (MEA). Also, we expect that the design of the strong interaction between Pt and CeO_x NW could be maximized by formation of the Pt-CeO_x interface. Then, the stability of the Pt-CeO_x interface would be improved. In our future work, the influence of dissolution of the Pt-CeO_x NW interface from the electrode layer of MEA on the fuel cell performance will be examined. In addition, we are going to maximize the Pt-CeO_x interface area on activated CeO_x NW by using high energy irradiation techniques. Through this challenge, it is expected that the design concept of the Pt-CeO_x NW interface for a lowering of Pt in the electrode layer of fuel cells will be established.

3.3. Characterization of Surface and Bulk Regions by Using a Combination of HXPS and EELS Analyses. To investigate the reasons why the promoting effect of the CeO_x NW surface is greater than for the CeO_x NP surface, HXPS and EELS analyses were performed for characterization of the surface and bulk regions of the electrocatalyst, respectively.

3.3.1. Characterization from Surface to Bulk by Using HXPS. In principle, the analysis depth of HXPS can be estimated as 21 nm (i.e., 3 (inelastic mean free path of photoelectrons from Ce 3d of CeO_2: 7 nm)). Therefore, in principle, it is possible to detect the bulk information on CeO_x NW by using HXPS. However, in practical measurement, the detectable amount of emitted photoelectrons is exponentially attenuated. HXPS analysis mainly detects surface information. Also, the bulk information on CeO_x NW is partially involved in the practical HXPS measurement. As a consequence of this, HXPS analysis is important to characterize the surface to some part of bulk regions of the electrocatalyst with the heterogeneous interface.

Figure 7(a) shows the Pt 4f spectrum of electrochemically pretreated 5 wt % Pt loaded CeO_x NW/C revealing two spin–

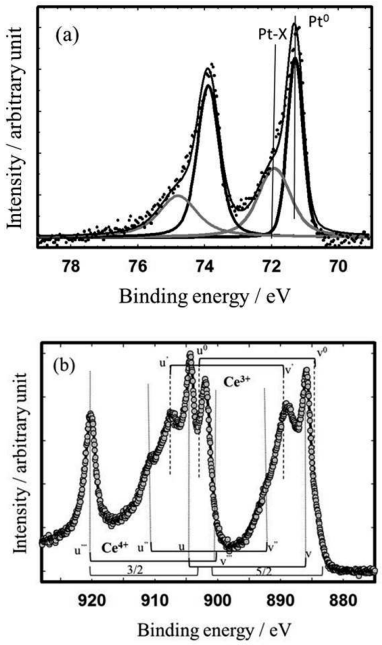

Figure 7. Pt 4f spectrum observed for 5 wt % Pt loaded CeO_x NW/C (a) after electrochemical pretreatment and Ce 3d spectrum observed for 5 wt % Pt loaded CeO_x NW/C (b) after electrochemical pretreatment.

orbital splitting doublets Pt $4f_{7/2}$-$4f_{5/2}$. The peak at 71.1 eV is a result of metallic Pt (Pt^0). The other extra peak located at a binding energy of 72.0 eV is labeled as Pt-X (X: O–Ce) and corresponds to slightly ionized Pt. This slightly ionized Pt peak which is located at midway between metallic Pt and Pt^{2+} (i.e., PtO, 72.6 eV[41]) is attributed to the formation of Pt–O–Ce bonds at the interface between Pt and CeO_x.[38−41] Note that the content of other ionized Pt species such as Pt^{2+} (i.e., PtO) and Pt^{4+} (i.e., PtO_2) was negligible in the present work and that the content of Pt-X (X: O–Ce) is large compared to Pt-CeO_x NP/C.[38,40]

The Ce 3d spectrum taken from the same sample is shown in Figure 7(b) where both Ce^{3+} (labeled as u^0, v^0, u′, and v′, where the symbols u and v are spin–orbital partners of $3d_{5/2}$ and $3d_{3/2}$, respectively) and Ce^{4+} (labeled as u, v, u″, v″, u‴, and v‴) can be observed. This spectrum suggests that the surface of 5 wt % Pt loaded CeO_x NW consists mainly of Ce^{4+} because of the large characteristic Ce^{4+} peak in the observed Ce 3d profile.

DOI: 10.1021/acsami.5b12469
ACS Appl. Mater. Interfaces 2016, 8, 9059–9070

Note that the number of peaks of Ce 3d observed for CeO_2 standard powder is usually just 6. In contrast, 7 peaks were observed for our 5 wt % Pt-CeO_x NW/C, as shown in Figure 7(b) (see Figures S4(a) and S4(b) of the Supporting Information). One extra peak in the Ce 3d profile which was observed for 5 wt % Pt loaded CeO_x NW/C appeared as well as the Pt 4f profile. The aforementioned two extra peaks in Pt 4f and Ce 3d profiles clearly suggest the strong interaction between Pt and CeO_x NW and formation of the Pt-CeO_x NW interface on 5 wt % Pt loaded CeO_x NW/C.

Table 6 summarizes the data from the ratio of Pt-X (X: O−Ce)/all Pt species (i.e, metallic Pt, Pt^{2+}, and Pt^{4+}) and the Ce^{3+}/Ce^{4+} ratio of 5 wt % Pt-CeO_x NW/C. For reference, the same two ratios observed for 5 wt % Pt-CeO_x NW/C by using SXPS in our previously reported work[41] are also shown in Table 6. Note that Pt^{2+} and Pt^{4+} species on 5 wt % Pt-CeO_x NW/C were under a detectable level. The combination analysis of SXPS and HXPS suggests that the Pt-X (X: O−Ce)/all Pt species (i.e, metallic Pt, Pt^{2+}, and Pt^{4+}) ratio derived from 5 wt % Pt-CeO_x NW/C is 0.27 to 0.30. On the other hand, previously reported Pt-X (X: O−Ce) ratios for all Pt species (i.e, metallic Pt, Pt^{2+}, and Pt^{4+}) of 20 wt % Pt loaded CeO_x NP/C were from 0.08 to 0.17.[38] This clearly indicates that the content of Pt-X (X:O−Ce) bonds in 5 wt % Pt-CeO_x NW/C is greater than for 20 wt % Pt loaded CeO_x NP/C. It is thus concluded that the formation of an interface between Pt and CeO_x NW is promoted on the CeO_x NW surface.

Table 6. Surface Chemical Composition of 5 wt % Pt-CeO_x NW/C[b]

	Pt-X (X: O−Ce)/all Pt species	Ce^{3+}/Ce^{4+}
surface characterization by SXPS	0.27[a]	0.33[a]
surface characterization by HXPS	0.30	0.16

[a]Pt-X/all Pt species and Ce^{3+}/Ce^{4+} ratios were estimated by using the original data of Pt 4f and Ce 3d which was published in ref 41. [b]All Pt species: metallic Pt, Pt^{2+}, and Pt^{4+}.

In addition, the Ce^{3+}/Ce^{4+} ratios obtained for 5 wt % Pt-CeO_x NW/C are less than 0.33. This value is much lower than previously reported for Pt-CeO_x NP (from 0.64 to 1.36).[40] This indicates that the Ce^{4+} content at the surface from the bulk region of CeO_x NW is at a relatively high level. Note that the Ce^{3+} species was the main component in the bulk region of Pt loaded CeO_x NP/C. This suggests that a unique heterodefect interface is formed on 5 wt % Pt-CeO_x NW/C and the ORR activity of Pt should be highly promoted by the Pt-CeO_x NW interface in 5 wt % Pt-CeO_x NW/C.

3.3.2. EELS Study. To characterize the microstructural features more extensively in the bulk region of the Pt-CeO_x NW interface that are formed on CeO_x NW, an EELS study was performed to determine both the redox state of CeO_x and oxygen vacancy ordering of CeO_x in the electrocatalyst sample.

Figure 8(a) presents the energy-loss near edge structure (ELNES) of the Ce $M_{4,5}$-edge for 5 wt % Pt-CeO_x NW/C which contains two sharp peaks close to the ionization threshold. It has been demonstrated that the intensity ratio of these sharp peaks, I_{M4}/I_{M5}, can be used to estimate the valence state of Ce, where approximate values of 1.25 and 0.95 indicate, respectively, Ce^{4+} and Ce^{3+} species.[34,49] The I_{M4}/I_{M5} ratio found from the data contained in Figure 8(a) is 0.96, close to the value for Ce^{3+}. This indicates that regions away from the surface, more into the bulk of 5 wt % Pt-CeO_x NW/C, consist mainly of Ce^{3+} species, although its surface to some of the bulk regions consists mainly of Ce^{4+} species. Since the I_{M4}/I_{M5} ratio estimated from CeO_x NW without Pt was 1.1 (see Figure S5(a) of the Supporting Information) which is close to the value for Ce^{4+}, it is concluded that the redox state of CeO_x in 5 wt % Pt-CeO_x NW/C is changed drastically by formation of the interface between Pt and CeO_x NW.

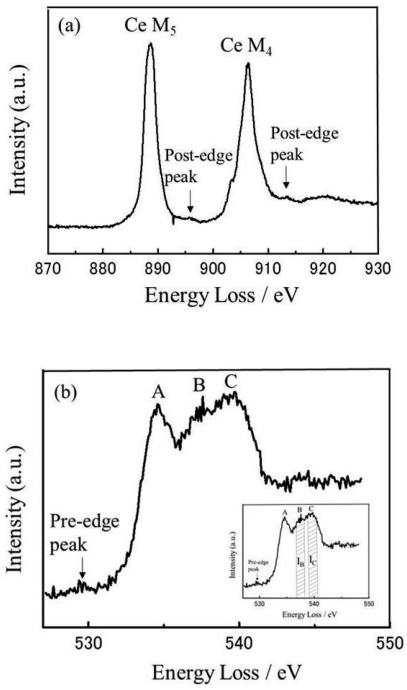

Figure 8. Cerium $M_{4,5}$-edge spectrum taken from electrochemically pretreated 5 wt % Pt-CeO_x NW/C (a) and oxygen K-edge spectrum taken from electrochemically pretreated 5 wt % Pt-CeO_x NW/C (b). Inset of part (b) shows the energy windows with 2 eV for calculating integral intensities of peaks B and C.

To further characterize the defect structural features of the bulk regions, the oxygen K-edge of the same sample was examined and is shown in Figure 8(b). After background subtraction, three main features labeled A, B, and C were observed above the threshold. Those were similar to the previously reported oxygen K-edge peaks derived from, for instance, Ln-doped CeO_2 samples (Ln: lanthanide such as trivalent cations La, Sm, Gd, Dy, and so on). Ou et al. characterized quantitatively the local ordering of oxygen vacancies in Ln doped CeO_2 samples by using the integrated intensity ratio of peaks B and C (i.e., I_B/I_C).[50] In their work, the large value of I_B/I_C indicated a high degree of local ordering of oxygen vacancies in Ln doped CeO_2 samples. The defects in their Ln-doped CeO_2 took up a Schottky defect structure, which was formed by dissolution of Ln into the CeO_2 lattice. The I_B/I_C ratio estimated from the data of Figure 8(b) was 0.75. Also, the I_B/I_C ratio taken from Ln-doped CeO_2 was 0.73 to 0.81. In addition, Fugane et al. have suggested Schottky defect structure formation at the Pt-CeO_x NP interface and simulated this by using atomistic simulation.[40] Both the estimated and previously reported I_B/I_C ratios of oxygen K-edge peaks suggest that the defect structure of CeO_x in 5 wt % Pt-CeO_x NW/C is Schottky type, having been formed by dissolution of Pt cations into the CeO_x lattice. Note that the relative intensity of peak B observed for pure CeO_2 without Ln

DOI: 10.1021/acsami.5b12469
ACS Appl. Mater. Interfaces 2016, 8, 9059−9070

dopant was considerably lower than Ln-doped CeO_2.[51] The same low intensity of peak B was observed in the present work for pure CeO_x NW containing no Pt (see Figure S5(b) of the Supporting Information). This is supported by the value of the I_B/I_C ratio of CeO_x in 5 wt % Pt-CeO_x NW/C.

Overall, based on these HXPS and EELS analyses, 5 wt % Pt-CeO_x NW/C contains a unique heterogeneous interface structure. In the region of the surface, 5 wt % Pt-CeO_x NW/C mainly contains Ce^{4+} species and Pt-X (X: O−Ce) species. In contrast, the bulk region consists mainly of Ce^{3+} species and Pt-X (X: O−Ce) species similarly to Pt-CeO_x NP/C. The surface region is different from the bulk of the 5 wt % Pt-CeO_x NW/C with high ORR activity. This heterogeneous interface structure should contribute to enhancement of the promoting effect of CeO_x NW on ORR activity of electrocatalysts with lower loadings of Pt on CeO_x NW.

4. DISCUSSION

Our experimental results have shown that the ORR activity of Pt is significantly enhanced by the formation of the Pt-CeO_x NW heterointerface leading us to conclude that this structural feature could play a key role in maximizing ORR activity on Pt and in minimizing Pt content of electrocatalysts contained in fuel cell devices.

To assist in the interpretation of the microanalytical results obtained for the Pt-CeO_x NW heterointerface and to consider the differences in Pt-oxide promotor interactions between CeO_x NW and CeO_x NP in the ORR reaction, we have also performed atomistic simulation of the Pt-CeO_x NW interface on Pt using interatomic potential and shell models.

EELS analysis of the bulk region suggests that Pt-CeO_x NW consists mainly of Ce^{3+} species and is of a Schottky defect structure similar to that found in Ln-doped CeO_2 samples. According to a similar atomistic simulation by Fugane et al.,[40] Schottky defect clusters are formed at the Pt-CeO_x NP interface by the following two empirical reactions

$$\mathrm{Pt} + 2\mathrm{Ce}_{\mathrm{Ce}^{x}_{e}} \xrightarrow{\mathrm{CeO_2}} \mathrm{Pt}_{\mathrm{Ce}}'' + 2\mathrm{V}_{\mathrm{o}}^{\bullet\bullet} + 2\mathrm{Ce}_{\mathrm{Ce}}' \quad (1)$$

$$2(\mathrm{Pt}_{\mathrm{Ce}}'' + 2\mathrm{V}_{\mathrm{o}}^{\bullet\bullet} + 2\mathrm{Ce}_{\mathrm{Ce}}') + 12(\mathrm{Pt}_{\mathrm{Ce}}'' + \mathrm{V}_{\mathrm{o}}^{\bullet\bullet}) \rightarrow \text{C-type rare earth like defect structure} \quad (2)$$

where the Kröger-Vink notation is used to explain the defect structure formation. In those defect formation reactions, Ce^{3+} cations are formed by dissolution of Pt^{2+} cations into the CeO_x lattice as a result of charge neutralization. Also, Schottky type oxygen vacancies are formed at the Pt-CeO_x NP interface. Our EELS analysis results taken from 5 wt % Pt-CeO_x NW/C agree with this defect formation model for Pt-CeO_x NP/C. Therefore, the defect structure in the bulk region of Pt-CeO_x NW/C is the same as that found in Pt-CeO_x NP/C. In contrast, the experimental data from HXPS indicates that the region from surface to bulk of 5 wt % Pt-CeO_x NW/C consists mainly of Pt-X (X: O−Ce) and Ce^{4+} components. Those results clearly indicate that the Pt-CeO_x NW interface in 5 wt % Pt-CeO_x NW/C consists of a unique heterogeneous structure. Bulk regions of the samples consist mostly of C-type rare earth like defect structures with Schottky defects. In contrast, a different defect structure was formed from the surface to the same part of the bulk region of the electrocatalysts.

Based on the result of HXPS analysis, we assume the following Frenkel defect structure formation at the surface region (eq 3)

$$\mathrm{PtO} + \mathrm{Ce}_{\mathrm{Ce}^{x}} + 4\mathrm{O}_{\mathrm{O}^{x}} + 6\mathrm{V}_{\mathrm{i}^{x}} \rightarrow 2\mathrm{Pt}_{\mathrm{i}}^{\bullet\bullet} + 4\mathrm{O}_{\mathrm{i}}'' + 4\mathrm{V}_{\mathrm{o}}^{\bullet\bullet} + \mathrm{V}_{\mathrm{Ce}}'''' + \mathrm{CeO}_2 \quad (3)$$

where the subscript character i means the interstitial site in the Kröger-Vink notation.

On the basis of this assumption, the stable configuration of Frenkel defect clusters in the unit cell of fluorite related CeO_x was estimated using atomistic simulation. If the calculated ΔE_b of the Frenkel defect cluster was at the highest level in all other configurations in the unit cell, our atomistic simulation predicts that the configuration of such a Frenkel defect cluster is stable in the unit cell.

The highest ΔE_b of the ($2Pt_I^{\bullet\bullet}$ - $4O_i''$ - $4V_o^{\bullet\bullet}$ - V_{Ce}'''') cluster in all possible configurations in the unit cell was 3.6 eV. Figure 9(a) shows the stable configuration of the ($2Pt_i^{\bullet\bullet}$ - $4O_i''$ - $4V_o^{\bullet\bullet}$ - V_{Ce}'''') cluster with the highest ΔE_b. To find more stable and larger Frenkel defect clusters at the Pt-CeO_x NW interface, we constructed the large Frenkel defect clusters as shown in Figures 9(b), 9(c), and 9(d). The calculated ΔE_b values based on the configuration of clusters shown in Figure 9 were 3.8, 3.9, and 6.6 eV, respectively, for clusters shown in Figure 9(b), 9(c), and Figure 9(d). The configuration of the large Frenkel defect cluster shown in Figure 9(d) is similar to the defect structure of the C-type rare earth structure.

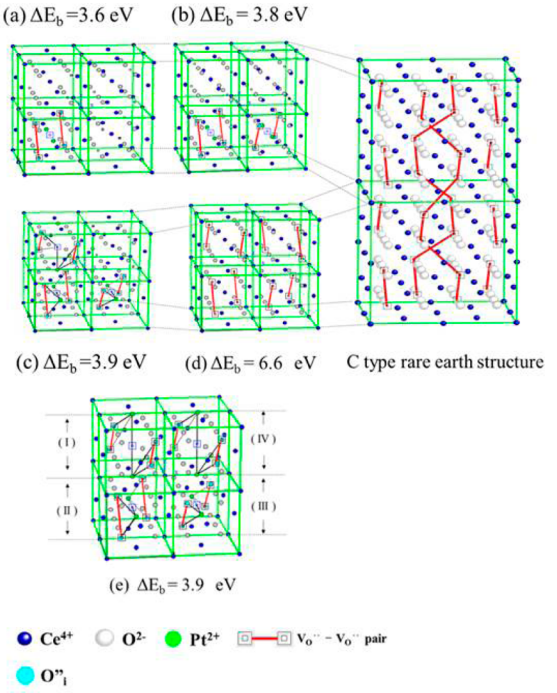

Figure 9. Schematic diagram of proposed Frenkel defect cluster structure in the Pt-CeO_x NW interface: (a) $2Pt_i^{\bullet\bullet}$ - $4O_i''$ - $4V_o^{\bullet\bullet}$ - V_{Ce}'''', (b) 2(a), (c) 3(a), (d) 4(a), and (e) modification of (d). ΔE_b is binding energy of cluster.

Alternatively, if the Frenkel defect positions of oxygen atoms were slightly different from those of the Schottky defect positions of oxygen vacancies in the C-type rare earth structure, high ΔE_b and stable cluster structures cannot be expected at the Pt-CeO_x NW interface. As a representative example, the configuration of Frenkel type oxygen defects was altered as shown in Figure 9(e). For this change, the Frenkel type oxygen defect positons in region IV are duplicated in region I (see

DOI: 10.1021/acsami.5b12469
ACS Appl. Mater. Interfaces 2016, 8, 9059−9070

Figure 9(e)). Note that this is not equivalent to oxygen defect configurations in the C-type rare earth structure as shown in empirical eq 4 and Figure 9(d)

$$4(2Pt_i^{\bullet\bullet} - 4O_i'' - 4V_o^{\bullet\bullet} - V_{Ce}'''') \rightarrow \text{C-type rare earth like defect structure} \quad (4)$$

The ΔE_b value calculated on the basis of the Frenkel model in Figure 9(e) was 3.9 eV. This is much lower than the ΔE_b calculated on the basis of the defect model shown in Figure 9(d) as demonstrated in Figure 10. Also, the ΔE_b value

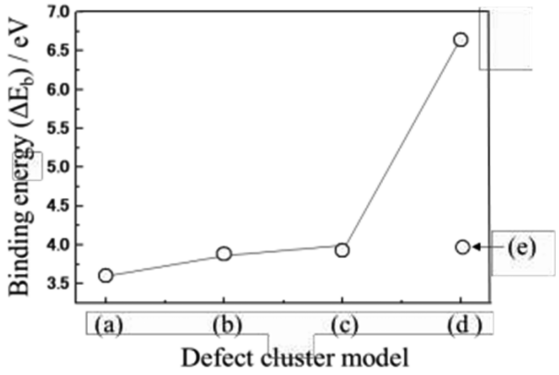

Figure 10. Calculated binding energies (ΔE_b) for deferent cluster models: (a) $2Pt_i^{\bullet\bullet}$ - $4O_i''$ - $4V_o^{\bullet\bullet}$ - V_{Ce}'''', (b) 2(a), (c) 3(a), (d) 4(a), and (e) modification of (d).

calculated on the basis of the Frenkel model in Figure 9 (d) was approximately 6 times greater than that of previously reported ΔE_b calculated based on a Schottky defect model for of the Pt-CeO_x NP/C system.[40] This suggests that these Frenkel defect clusters (i.e. $2Pt_i^{\bullet\bullet}$ - $4O_i''$ - $4V_o^{\bullet\bullet}$ - V_{Ce}'''') are widely formed from the surface to some part of bulk regions of the Pt-loaded CeO_x NW interface as illustrated in Figure 11. Also, our atomistic simulation suggests that diffusion of Pt^{2+} cations from the Pt particle into the Frenkel site of the fluorite CeO_x lattice contributed to the formation of heterogeneous clusters which consist of interstitial site oxygen (O_i), oxygen vacancy ($V_o^{\bullet\bullet}$), and cerium defect (V_{Ce}'''') .

Some of our collaborative team members simulated the surface defect structure of CeO_x using our simulation method before.[45] In this previously published work, the surface defect structure was simulated from the first surface layer to the sixth surface layer by using large scale calculation. In this calculation, a number of oxygen atoms shifted to interstitial sites, and shifted oxygen atoms crated large defect clusters which are associated with Ce^{3+} cations. It is well known that the surface defect cluster formation is more complicated as compared to that in the bulk. However, the authors used more simple calculation ways for our discussion on the basis of observed HXPS data and EELS data since HXPS analysis shows both surface and some part of bulk information and TEM-EELS analysis tells us bulk information. Therefore, we selected the simple calculation method for conclusion of features about the interface defect structure which is a little bit far from the surface. Note that our atomistic simulation in the present work was performed for an interpretation of the results of HXPS and TEM-EELS analyses for development of our design concept.

Our atomistic simulation suggests that the charge transfer phenomena on the surface of Pt-CeO_x NW/C electrocatalysts were improved by Pt^{2+} cations contained in the Frenkel defect clusters. Also, both Frenkel type oxygen defects formed by interaction of Pt-CeO_x NW and surface oxygen and cerium defects should be easily formed at the surface. The formation of Frenkel type oxygen defects would contribute to the increased affinity for oxygen molecules at the surface of these electrocatalysts. In the bulk region of the electrocatalyst, the electrochemical redox reaction between Ce^{3+} and Ce^{4+} operates similarly to that for Pt loaded CeO_x NP electrocatalysts, as has been suggested by Masuda et al.[37] It is concluded that ORR activity on Pt is maximized by a combination of the promoting effect caused by the presence of both Frenkel and Schottky defects at the Pt-CeO_x NW interface.

We conclude that surface modification and activation of CeO_x NW will be a key in the development of ultralow-Pt cathodes. This will require the optimization of the role of the CeO_x NW promotor with an associated minimization of the Pt content of electrocatalysts for effective ORR and superior implementation of the fuel cell reaction.

5. CONCLUSION

The Pt-CeO_x NW interaction could take place in the Pt-CeO_x NW interface for promotion of ORR activity on Pt in fuel cell reaction. The Pt loaded CeO_x NW interface consists of a unique heterogeneous structure. Frenkel type defect clusters which would contribute to the enhancement of both charge transfer and affinity for oxygen molecules at the surface were formed from the surface to some part of the bulk regions. Also, Schottky type defect clusters, in which the electrochemical redox reaction between Ce^{3+} and Ce^{4+} operated similarly to that for Pt loaded CeO_x NP electrocatalysts, were formed in the bulk region. As a result, the Tafel slope of 5 wt % Pt-CeO_x NW/C became steep as compared to 5 wt % Pt-CeO_x NP/C. It indicates that the promotion effect of the CeO_x NW surface became much higher than that of the CeO_x NP surface. Also, the observed ORR activity on Pt in Pt-CeO_x NW/C was dramatically improved by the formation of this unique heterointerface.

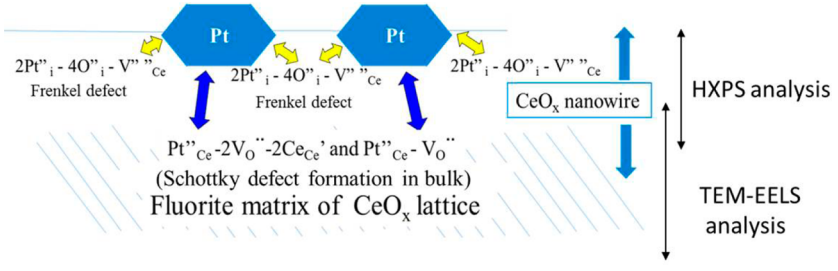

Figure 11. Schematic diagram of heterogeneous interface which was formed between Pt and CeO_x NW.

DOI: 10.1021/acsami.5b12469
ACS Appl. Mater. Interfaces 2016, 8, 9059−9070

However, a small amount of the Pt-CeO_x NW interface would be dissolved in an acidic solution in 1000 cycle sweeps of the long cycle test. We expect that the design of strong interaction between Pt and CeO_x NW could be maximized by formation of the Frenkel type defect cluster ($2Pt_i^{\bullet\bullet}$ - $4O_i''$ - $4V_o^{\bullet\bullet}$ - V_{Ce}'''') in the Pt-CeO_x interface. Then, the stability of the Pt-CeO_x interface would be improved. Accordingly, the Frenkel defect cluster design on CeO_x NW support will be key in order to minimize Pt content in the electrocatalyst and maximize the ORR activity of Pt in the fuel cell reactions.

■ ASSOCIATED CONTENT

Supporting Information

The Supporting Information is available free of charge on the ACS Publications website at DOI: 10.1021/acsami.5b12469.

SEM photographs taken from as prepared CeO_x NW and 5 wt % Pt loaded CeO_x NW/C before electrochemical pretreatment. CV and particle size distribution data taken from 5 wt % Pt loaded CeO_x NW/C. Tafel plots comparison among 20 wt % Pt/C, 5 wt % Pt-CeO_x NW/C, and 20 wt % Pt-CeO_x NP/C. Ce 3d profiles for comparison between CeO_2 standard powder and Pt loaded CeO_x NW/C. EELS data observed for pure CeO_x NW without Pt (PDF)

■ AUTHOR INFORMATION

Corresponding Author

*Phone: 81-29-860-4395. Fax: 81-29-860-4712. E-mail: MORI.Toshiyuki@nims.go.jp.

Funding

The present work was partially supported by the Grant-in Aid for Scientific Research (Fundamental Research B (No. 25281066) by the Ministry of Education, Culture, Sports, and Technology (MEXT), Japan. Also, our work was partially supported by the Global Research Center for Environmental and Energy based on the Nanomaterials Science (GREEN), National Institute for Materials Science (NIMS), Japan.

Notes

The authors declare no competing financial interest.

■ ACKNOWLEDGMENTS

The authors express sincere gratitude to Mr. Keiji Kurashima, Ms. Kanako Nakayashiki of the TEM station of NIMS (Japan), and Professor Jin Zou of Centre for Microscopy and Microanalysis of The University of Queensland (Australia), for their assistance with microanalyses. The HXPS experiments were performed under the approval of NIMS Synchrotron X-ray Beamline Station (Proposal No. 2014B4600). The authors are grateful for operational support from Mr. Yoshitomo Shimada and Mr. Satoshi Ishimaru at BL15XU of SPring8. In addition, the authors greatly appreciate the useful advice regarding atomistic simulations given by Dr. Keisuke Fugane and Professor Fei Ye. The authors declare that part of the data (i.e., Tables 1 and 2 in 2. Experimental Section and Figures 9 and 10 in 4. Discussion section) was shown in the thesis manuscript of Dr. Shipra Chauhan (i.e., the first name author of the present manuscript). Those were already published as an electric version at the following Web site: http://hdl.handle.net/2115/59431.

■ REFERENCES

(1) Springer, T. E.; Zowodzinski, T. A.; Gottesfeld, S. Polymer Electrolyte Fuel Cell Model. *J. Electrochem. Soc.* **1991**, *138*, 2334−2342.

(2) Kordesch, K. V.; Simader, G. R. Environmental Impact of Fuel Cell Technology. *Chem. Rev.* **1995**, *95*, 191−207.

(3) Steele, B. C. H.; Heinzel, A. Materials for Fuel-cell Technologies. *Nature* **2001**, *414*, 345−352.

(4) Gong, K.; Du, F.; Xia, Z.; Durstock, M.; Dai, L. Nitrogen-doped Carbon Nanotube Arrays with High Electrocatalytic Activity for Oxygen Reduction. *Science* **2009**, *323*, 760−764.

(5) Lin, L.; Zhu, Q.; Xu, A.-W. Noble-Metal-Free Fe-N/C Catalyst for Highly Efficient Oxygen Reduction Reaction under Both Alkaline and Acidic Conditions. *J. Am. Chem. Soc.* **2014**, *136*, 11027−11033.

(6) Liu, D.; Zhang, X.; Sun, Z.; You, T. Free-standing Nitrogen-doped Carbon Nanofiber Film as Highly Efficient Electrocatalysts for Oxygen Reduction. *Nanoscale* **2013**, *5*, 9528−9531.

(7) Qu, L.; Liu, Y.; Baek, J.-B.; Dai, L. Nitrogen-doped Graphene as Efficient Metal-free Electrocatalyst for Oxygen Reduction in Fuel Cells. *ACS Nano* **2010**, *4*, 1321−1326.

(8) Yang, S.; Feng, X.; Wang, X.; Mullen, K. Graphene-based Carbon Nitride Nanosheets as Efficient Metal-free Electrocatalysts for Oxygen Reduction Reactions. *Angew. Chem., Int. Ed.* **2011**, *50*, 5339−5343.

(9) Yang, Z.; Yao, Z.; Li, G.; Fang, G.; Nie, H.; Liu, Z.; Zhou, X.; Chen, X.; Huang, S. Sulfur-doped Graphene as an Efficient Metal-free Cathode Catalyst for Oxygen Reduction. *ACS Nano* **2012**, *6*, 205−211.

(10) Zhang, Y. J.; Fugane, K.; Mori, T.; Niu, L.; Ye, J. Wet Chemical Synthesis of Nitrogen-doped Graphene towards Oxygen Reduction Electrocatalysts without High-temperature Pyrolysis. *J. Mater. Chem.* **2012**, *22*, 6575−6580.

(11) Tian, G.-L.; Zhang, Q.; Zhang, B.; Jin, Y.-G.; Huang, J.-Q.; Su, D. S.; Wei, F. Toward Full Exposure of "Active Sites": Nanocarbon Electrocatalyst with Surface Enriched Nitrogen for Superior Oxygen Reduction and Evolution Reactivity. *Adv. Funct. Mater.* **2014**, *24*, 5956−5961.

(12) Anderson, A. B. O_2 Reduction and CO Oxidation at the Pt-electrolyte Interface. The Role of H_2O and OH adsorption bond strengths. *Electrochim. Acta* **2002**, *47*, 3759−3763.

(13) Lin, S.-P.; Wang, K.-W.; Liu, C.-W.; Chen, H.-S.; Wang, J.-H. Trends of Oxygen Reduction Reaction on Platinum Alloys: A Computational and Experimental Study. *J. Phys. Chem. C* **2015**, *119*, 15224−15231.

(14) Wakisaka, M.; Suzuki, H.; Mitsui, S.; Uchida, H.; Watanabe, M. Identification and Quantification of Oxygen Species Adsorbed on Pt(111) Single-crystal and Polycrystalline Pt Electrodes by Photoelectron Spectroscopy. *Langmuir* **2009**, *25*, 1897−1900.

(15) Imai, H.; Izumi, K.; Matsumoto, M.; Kubo, Y.; Kato, K.; Imai, Y. In Situ and Real-time Monitoring of Oxide Growth in a Few Monolayer at Surfaces of Platinum Nanoparticles in Aqueous Media. *J. Am. Chem. Soc.* **2009**, *131*, 6293−6300.

(16) Tseung, A. C. C.; Dhara, S. C. Loss of Surface Area by Platinum and Supported Platinum Black Electrocatalyst. *Electrochim. Acta* **1975**, *20*, 681−683.

(17) Honji, A.; Mori, T.; Tamura, K.; Hishinuma, Y. Agglomeration of Platinum Particles Supported on Carbon in Phosphoric Acid. *J. Electrochem. Soc.* **1988**, *135*, 355−359.

(18) Shim, J.; Lee, C.-R.; Lee, H.-K.; Lee, J.-S.; Cairns, E. J. Electrochemical Characteristics of Pt-WO_3/C and Pt-TiO_2/C Electrocatalysts in a Polymer Electrolyte Fuel Cell. *J. Power Sources* **2001**, *102*, 172−177.

(19) Yan, Z.; Wei, W.; Xie, J.; Meng, S.; Lu, X.; Zhu, J. An Ion Exchange Route to Produce WO_3 Nanobars as Pt Electrocatalyst Promoter for Oxygen Reduction Reaction. *J. Power Sources* **2013**, *222*, 218−224.

(20) Yan, Z.; Xie, J.; Jing, J.; Zhang, M.; Wei, W.; Yin, S. MoO_2 Nanocrystals Down to 5 nm as Pt Electrocatalyst Promoter for Stable Oxygen Reduction Reaction. *Int. J. Hydrogen Energy* **2012**, *37*, 15948−15955.

DOI: 10.1021/acsami.5b12469
ACS Appl. Mater. Interfaces 2016, 8, 9059−9070

(21) Sasaki, K.; Zhang, L.; Adzic, R. R. Niobium Oxide-supported Platinum Ultra-low Amount Electrocatalysts for Oxygen Reduction. *Phys. Chem. Chem. Phys.* **2008**, *10*, 159−167.
(22) Okanishi, T.; Matsui, T.; Takeguchi, T.; Kikuchi, R.; Eguchi, K. Chemical Interaction between Pt and SnO_2 and influence on Adsorptive Properties of Carbon Monoxide. *Appl. Catal., A* **2006**, *298*, 181−187.
(23) Parrondo, J.; Mijangos, F.; Rambabu, B. Platinum/tin Oxide/carbon Cathode Catalyst for High Temperature PEM Fuel Cell. *J. Power Sources* **2010**, *195*, 3977−3983.
(24) Xu, C. W.; Shen, P. K. Novel Pt/CeO_2/C Catalysts for Electrooxidation of Alcohols in Alkaline Media. *Chem. Commun.* **2004**, 2238−2239.
(25) Xu, C. W.; Shen, P. K. Electrochemical Oxidation of Ethanol on Pt-CeO_2/C Catalysts. *J. Power Sources* **2005**, *142*, 27−29.
(26) Xu, C. W.; Zeng, R.; Shen, P. K.; Wei, Z. Synergistic Effect of CeO_2 Modified Pt/C Catalysts on the Alcohols Oxidation. *Electrochim. Acta* **2005**, *51*, 1031−1035.
(27) Takahashi, M.; Mori, T.; Vinu, A.; Kobayashi, H.; Drennan, J.; Ou, D. R. Preparation and Anode Property of Pt-CeO_2 Electrodes Supported on Carbon Black for Direct Methanol Fuel Cell Applications. *J. Mater. Res.* **2006**, *21*, 2314−2322.
(28) Takahashi, M.; Mori, T.; Ye, F.; Vinu, A.; Kobayashi, H.; Drennan, J. Design of High-Quality Pt-CeO_2 Composite Anodes Supported by Carbon Black for Direct Methanol Fuel Cell Application. *J. Am. Ceram. Soc.* **2007**, *90*, 1291−1294.
(29) Takahashi, M.; Mori, T.; Vinu, A.; Ou, D. R.; Kobayashi, H.; Drennan, J. Development of High Quality Pt-CeO_2 Electrodes Supported on Carbon Black for Direct Methanol Fuel Cell Applications. *Adv. Appl. Ceram.* **2008**, *107*, 57−63.
(30) Yu, H. B.; Kim, J. H.; Lee, H. I.; Scibioh, M. A.; Lee, J.; Han, J.; Yoon, S. P.; Ha, H. Y. Development of Nanophase CeO_2-Pt/C Cathode Catalyst for Direct Methanol Fuel Cell. *J. Power Sources* **2005**, *140*, 59−65.
(31) Takahashi, M.; Mori, T.; Yoshikawa, H.; Togasaki, K.; Fugane, A.; Tada, A.; Matolin, V.; Drennan, J. Influence of Pt and CeO_2 Interaction in Pt-CeO_2 Electrode on Anode and Cathode Performance for Fuel Cell Applications. *Trans. Mater. Res. Soc. Jpn.* **2008**, *33*, 1101−1104.
(32) Lim, D.-H.; Lee, W. − D.; Choi, D.-H.; Kwon, H.-H.; Lee, H.-I. The Effect of Cerium Oxide Nanoparticles on a Pt/C Electrocatalyst Synthesized by a Continuous Two-step Process for Low-temperature Fuel Cell. *Electrochem. Commun.* **2008**, *10*, 592−596.
(33) Lim, D.-H.; Lee, W. − D.; Choi, D.-H.; Lee, H.-I. Effect of Ceria Nanoparticles into the Pt/C Catalyst as Cathode Material on the Electrocatalytic Activity and Durability for Low-temperature Fuel Cell. *Appl. Catal., B* **2010**, *94*, 85−96.
(34) Ou, D. R.; Mori, T.; Togasaki, H.; Takahashi, M.; Ye, F.; Drennan, J. Microstructural and Metal-support Interactions of the Pt-CeO_2/C Catalysts for Direct Methanol Fuel Cell Application. *Langmuir* **2011**, *27*, 3859−3866.
(35) Ou, D. R.; Mori, T.; Fugane, K.; Togasaki, H.; Ye, F.; Drennan, J. Stability of Ceria Supports in Pt-CeO_x/C Catalysts. *J. Phys. Chem. C* **2011**, *115*, 19239−19245.
(36) Mori, T.; Ou, D. R.; Zou, J.; Drennan, J. Present status and future prospect of design of Pt-cerium oxide electrodes for fuel cell applications. *Prog. Nat. Sci.* **2012**, *22*, 561−571.
(37) Masuda, T.; Fukumitsu, H.; Fugane, K.; Togasaki, H.; Matsumura, D.; Tamura, K.; Nishihata, Y.; Yoshikawa, H.; Kobayashi, K.; Mori, T.; Uosaki, K. Role of Cerium Oxide in the Enhancement of Activity for the Oxygen Reduction Reaction at Pt-CeO_x Nanocomposite Electrocatalyst - An In Situ Electrochemical X-ray Absorption Fine Structure Study. *J. Phys. Chem. C* **2012**, *116*, 10098−10102.
(38) Fugane, K.; Mori, T.; Ou, D. R.; Suzuki, A.; Yoshikawa, H.; Masuda, T.; Uosaki, K.; Yamashita, Y.; Ueda, S.; Kobayashi, K.; Okazaki, N.; Matolinova, I.; Matolin, V. Activity of Oxygen Reduction Reaction on Small Amount of Amorphous CeO_x Promoted Pt Cathode for Fuel Cell Application. *Electrochim. Acta* **2011**, *56*, 3874−3883.
(39) Fugane, K.; Mori, T.; Ou, D. R.; Yan, P. F.; Yoshikawa, H.; Drennan, J. Improvement of Cathode Performance on Pt-CeO_x by Optimization of Electrochemical Pretreatment Condition for PEFC Application. *Langmuir* **2012**, *28*, 16692−16700.
(40) Fugane, K.; Mori, T.; Yan, P. F.; Masuda, T.; Yamamoto, S.; Ye, F.; Yoshikawa, H.; Auchterlonie, G.; Drennan, J. Defect Structure Analysis of Hetero-interface between Pt and CeO_x Promoter on Pt Electrocatalyst. *ACS Appl. Mater. Interfaces* **2015**, *7*, 2698−2707.
(41) Chauhan, S.; Richards, G. J.; Mori, T.; Yan, P. F.; Hill, J. P.; Ariga, K.; Drennan, J. Fabrication of a Nano-structured Pt-loaded Cerium Oxide Nanowire and Its Anode Performance in the Methanol Electro-oxidation Reaction. *J. Mater. Chem. A* **2013**, *1*, 6262−6270.
(42) Tanuma, S.; Powell, C. J.; Penn, D. R. Calculations of Electron Inelastic Mean Free Paths. *Surf. Interface Anal.* **1994**, *21*, 165−176.
(43) Ueda, S.; Katsuya, Y.; Tanaka, M.; Yoshikawa, H.; Yamashita, Y.; Ishimaru, S.; Matsushita, Y.; Kobayashi, K. Present Status of the NIMS Contract Beamline BL15XU at SPring-8. *AIP Conf. Proc.* **2009**, *1234*, 403−406.
(44) Ueda, S. Application of Hard X-ray Photoelectron Spectroscopy to Electronic Structure Measurements for Various Functional Materials. *J. Electron Spectrosc. Relat. Phenom.* **2013**, *190*, 235−241.
(45) Ma, J. L.; Ye, F.; Ou, D. R.; Li, L. L.; Mori, T. Structures of Defect Clusters on Ceria {111} Surface. *J. Phys. Chem. C* **2012**, *116*, 25777−25782.
(46) Vyas, S.; Grimes, R. W.; Gay, D. H.; Rohl, A. L. Structure. Stability and Morphology of Stoichiometric Ceria Crystallites. *J. Chem. Soc., Faraday Trans.* **1998**, *94*, 427−434.
(47) Gale, J. D. GULP: A Computer Program for the Symmetry-adapted Simulation of Solids. *J. Chem. Soc., Faraday Trans.* **1997**, *93*, 629−637.
(48) Markovic, N. M.; Gasteiger, H. A.; Ross, P. N. Oxygen Reduction on Platinum Low-index Single-crystal Surfacs in Sulfuric Acid Solution: Rotating Ring-Pt(hkl) Disk Studies. *J. Phys. Chem.* **1995**, *99*, 3411−3415.
(49) Arai, S.; Muto, S.; Murai, J.; Sasaki, T.; Kuroda, K.; Saka, H. Valence Change of Cations in Ceria-zirconia Solid Solution Associated eith Redox Reactions Studied with Electron Energy-loss Spectroscopy. *Mater. Trans.* **2004**, *45*, 2951−2955.
(50) Ou, D. R.; Mori, T.; Ye, F.; Zou, J.; Drennan, J. Oxygen-vacancy Ordering in Lanthanide-doped Ceria: Dopant-type Dependence and Structure Model. *Phys. Rev. B: Condens. Matter Mater. Phys.* **2008**, *77*, No. 024108.
(51) Ou, D. R.; Mori, T.; Ye, F.; Kobayashi, T.; Zou, J.; Auchterlonie, G.; Drennan, J. Oxygen Vacancy Ordering in Heavily Rare Earth-doped Ceria. *Appl. Phys. Lett.* **2006**, *89*, 171911.

DOI: 10.1021/acsami.5b12469
ACS Appl. Mater. Interfaces 2016, 8, 9059−9070